The Astrophysical Journal, 723:104–115, 2010 November 1 doi:10.1088/0004-637X/723/1/104

THE WFC3 INFRARED SPECTROSCOPIC PARALLEL (WISP) SURVEY*

H. Atek[1], M. Malkan[2], P. McCarthy[3], H. I. Teplitz[4], C. Scarlata[1], B. Siana[5], A. Henry[6], J. W. Colbert[1], N. R. Ross[2], C. Bridge[5], A. J. Bunker[7], A. Dressler[3], R. A. E. Fosbury[8], C. Martin[6], and H. Shim[1]
[1] Spitzer Science Center, Caltech, Pasadena, CA 91125, USA
[2] Department of Physics and Astronomy, University of California, Los Angeles, CA 90024, USA
[3] Observatories of the Carnegie Institution for Science, Pasadena, CA 91101, USA
[4] Infrared Processing and Analysis Center, Caltech, Pasadena, CA 91125, USA
[5] Department of Astronomy, Caltech, Pasadena, CA 91125, USA
[6] Department of Physics, University of California, Santa Barbara, CA 93106, USA
[7] Department of Physics, University of Oxford, Denys Wilkinson Building, Keble Road, OX13RH, UK
[8] Space Telescope-European Coordinating Facility, Garching bei München, Germany
Received 2010 May 21; accepted 2010 August 27; published 2010 October 7

ABSTRACT

We present the WFC3 Infrared Spectroscopic Parallel (WISP) Survey. WISP is obtaining slitless, near-infrared grism spectroscopy of ∼90 independent, high-latitude fields by observing in the pure-parallel mode with the Wide Field Camera Three on the *Hubble Space Telescope* for a total of ∼250 orbits. Spectra are obtained with the G_{102} ($\lambda = 0.8$–$1.17\,\mu$m, $R \sim 210$) and G_{141} grisms ($\lambda = 1.11$–$1.67\,\mu$m, $R \sim 130$), together with direct imaging in the J and H bands (F110W and F140W, respectively). In the present paper, we present the first results from 19 WISP fields, covering approximately 63 arcmin^2. For typical exposure times (∼6400 s in G_{102} and ∼2700 s in G_{141}), we reach 5σ detection limits for emission lines of $f \sim 5 \times 10^{-17}$ erg s^{-1} cm^{-2} for compact objects. Typical direct imaging 5σ limits are 26.3 and 26.1 mag. (AB) in F110W and F140W, respectively. Restricting ourselves to the lines measured with the highest confidence, we present a list of 328 emission lines, in 229 objects, in a redshift range $0.3 < z < 3$. The single-line emitters are likely to be a mix of Hα and [O III]5007,4959 Å, with Hα predominating. The overall surface density of high-confidence emission-line objects in our sample is approximately 4 per arcmin^2. These first fields show high equivalent width sources, active galactic nucleus, and post-starburst galaxies. The median observed star formation rate (SFR) of our Hα-selected sample is 4 $M_\odot$ yr^{-1}. At intermediate redshifts, we detect emission lines in galaxies as faint as $H_{140} \sim 25$, or $M_R < -19$, and are sensitive to SFRs down to less than 1 $M_\odot$ yr^{-1}. The slitless grisms on WFC3 provide a unique opportunity to study the spectral properties of galaxies much fainter than L^* at the peak of the galaxy assembly epoch.

Key words: galaxies: distances and redshifts – galaxies: statistics – infrared: galaxies – surveys

Online-only material: color figures

1. INTRODUCTION

While there is considerable uncertainty regarding the detailed star formation history of galaxies of various masses and types, it has become clear that the span of cosmic time $0.5 \leqslant z \leqslant 2.5$ encompasses most of the star formation in the history of the universe (e.g., Hopkins 2004; Daddi et al. 2007). This broad epoch is also when many galaxies were "assembled," when major mergers and the accretion of satellite galaxies and gas combined to produce the variety of morphologies and structures of modern galaxies. There is mounting evidence for an evolution of star-forming galaxies during this time period, from high-mass galaxies dominating at $z \sim 3$ to low-mass galaxies at the present. Deep, wide IR surveys are required to cover much of the peak epoch of star formation, because of the redshifting of the key diagnostic spectral features of stellar evolution, and to minimize the effect of obscuration by dust.

The difficulty of obtaining observed-frame near-infrared spectra causes much of our empirical perspective on galaxy evolution to be biased by the way in which spectroscopic samples are selected. Color selection reliably selects common objects, but misses unexpected ones; magnitude-limited samples necessarily favor bright-continuum objects. Ground-based searches for emission lines from faint high-redshift galaxies are severely impacted by the bright NIR airglow. Excluding OH terrestrial airglow frequencies restricts redshift coverage and compromises redshift identification. Space-based spectroscopic surveys offer significant advantages for unbiased target selection. The grisms on the Near Infrared Camera and Multi Object Spectrometer (NICMOS), the Space Telescope Imager and Spectrograph (STIS), and the Advanced Camera for Survey (ACS) have demonstrated the power of spectroscopy from above the atmosphere, where the low background emission permits slitless observing (Gardner et al. 1998; McCarthy et al. 1999; Teplitz et al. 2003a; Pirzkal et al. 2004; Drozdovsky et al. 2005). Furthermore, the terrestrial wavelength gaps can only be filled from space, as first demonstrated by the pure-parallel program with the NICMOS G_{141} grism (McCarthy et al. 1999; Yan et al. 2000; Shim et al. 2009).

Much as ground-based objective prism surveys (e.g., Gallego et al. 1996) were used to define flux-limited samples of Hα emitters at $z \sim 0$, the NICMOS grism observations produced complete samples of emission-line objects at intermediate redshifts. Yan et al. (1999) and Hopkins et al. (2000) used observations with the NICMOS H-band (G_{141}) grism to derive Hα luminosity functions, and to show that the luminosity density, and hence star formation rate (SFR) density, has evolved

* Based on observations made with the NASA/ESA *Hubble Space Telescope*, which is operated by the Association of Universities for Research in Astronomy, Inc., under NASA contract NAS 5-26555. These observations are associated with program 11696.

by a factor of ∼10 from $z \sim 1.4$ to the present. Shim et al. (2009) used a larger sample to derive improved Hα luminosity functions in two redshift bins and confirmed the trends seen in the analysis by Yan et al. and Hopkins et al. The complete reductions/extractions of grism data for the principal modes of NICMOS were released in the *Hubble* Legacy Archive (HLA; Freudling et al. 2008). Nearly all of the published results from the NICMOS grisms were based on data with the G_{141} H-band disperser. The poor sensitivity of the NICMOS detector at short wavelengths limited the utility of the G_{102} grism.

The grisms on ACS have been used to discover faint Lyα emission sources and faint Lyman continuum break sources at $z \sim 3$–4 (Malhotra et al. 2005; Pirzkal et al. 2007) as well as to derive spectrophotometric redshifts for a large sample of faint galaxies (e.g., Straughn et al. 2008, 2009). Extremely deep ACS grism observations have shown the power of low-resolution spectroscopy above the atmosphere to detect spectral breaks indicative of passively evolving systems (e.g., Daddi et al. 2005) or active star-forming galaxies (Pirzkal et al. 2004; Rhoads et al. 2005; Malhotra et al. 2005; Pasquali et al. 2006). The full release of the reduced ACS grism data in the HLA is underway (Kuemmel et al. 2009b). The STIS slitless modes work at higher resolution than the NICMOS and ACS grisms, but the relatively low sensitivity of STIS has limited its ability to sample populations beyond the reach of ground-base spectroscopic surveys (Teplitz et al. 2003b).

Wide Field Camera Three (WFC3) on *Hubble* has a larger field of view, significantly better detectors and superior sampling compared to camera 3 on NICMOS. The net improvement in survey speed is approximately a factor of 20. This enhanced survey speed does not fully capture the gains provided by WFC3. The quality of the spectra, in terms of resolution, a well-focused point-spread function (PSF), and uniform sensitivity are also greatly superior to those offered by NICMOS.

In *Hubble Space Telescope's* (*HST's*) Cycle 17, we began a new observing program of WFC3 pure parallels, the WFC3 Infrared Spectroscopic Parallel (WISP) survey. In ∼250 orbits, the program will obtain near-infrared slitless spectroscopy of ∼90 uncorrelated high-latitude fields (PI = Malkan, GO-11696). This will produce a large sample of emission-line galaxies to measure the SFR continuously from at $z \sim 0.5$ to $z \sim 2.5$, over which ground-based searches are severely limited. The study of dust and metallicity in a large, unbiased sample of galaxies and the evolution of the star formation density are among the main goals of our project. In this paper, we present the analysis of the first 19 fields from which we have selected high-confidence emission lines. In Sections 2 and 3, we describe the survey and data reduction. We discuss the results in Section 4, and finally offer some thoughts on the future possibilities in Section 5. Throughout, we assume a Λ-dominated flat universe, with $H_0 = 71$ km s^{-1} Mpc^{-1}, $\Omega_\Lambda = 0.73$, and $\Omega_m = 0.27$. All magnitudes are in AB system.

2. OBSERVATIONS

The infrared channel of the WFC3 utilizes a 1K× 1K HgCdTe detector array. At a plate scale of 0.13 arcsec pixel^{-1}, the total field of view covered is $123'' \times 136''$. There are two IR grisms on WFC3: G_{102} covering the 0.8–1.1 μm range with a dispersion of 0.0024 μm pixel^{-1} and G_{141} covering the 1.07–1.7 μm range with a dispersion of 0.0046 μm pixel^{-1}. These correspond to average resolving powers for point sources of $R = 210$ for the G_{102} and $R = 130$ for the G_{141}. For an unresolved line, the FWHM will be about 2 pixels. The details of the grisms and their characteristics can be found in Kimble et al. (2008) and on the WFC3 Web site.[9]

Each target field was observed briefly in direct imaging mode, using the broadband filter that matches the grism spectral coverage most closely: F110W for the G_{102}, and F140W for the G_{141}. As detailed in the next section, all of our observations were carried out in the "pure-parallel" mode with the Cosmic Origins Spectrograph (COS) or STIS operating as the prime instrument.

2.1. Pure-parallel Observation Scheduling

Pure-parallel observing with *HST* works as follows: observing programs approved on COS and STIS constitute a parallel-observing "opportunity" (see Table 1). Observations with these two instruments, by necessity, require stable, long integrations, which means that the entire focal plane of *HST* is held at a single pointing and fixed orientation angle for long periods of time. Thus, it is simply a matter of turning on one of the other instruments in the focal plane to obtain quality data in a parallel field, offset by a 5.′5 and 4.′75 from the COS and STIS primary target, respectively. This motivated the strategy of a number of programs using WFC3 in parallel. Two other *HST* Cycle 17 programs were approved, both to perform infrared direct imaging (GO-11702, PI = Yan; GO-11700 PI = Trenti). Pure-parallel observing is perfectly suited to the goals of the WISP Survey, since it allows us to obtain deep, continuous, IR spectroscopy in dozens of uncorrelated fields.

We selected our parallel targets with a preference for long integration times and high-galactic-latitude (>30 degrees out of the galactic plane) fields. In order to reach similar depths in both the G_{102} and G_{141} spectra, we planned an ∼2.5:1 G_{102}:G_{141} integration time ratio. Additionally, the process of extracting the slitless spectra from the grism images requires direct imaging of the same fields (see Section 3) and so we obtained imaging in F110W and F140W (corresponding to J_{110} and H_{140} band, respectively) on the same orbits as the grism imaging with an ∼6:1 grism:direct imaging integration time ratio. To date, we have received, reduced, and analyzed 19 fields (Table 1), the results of which are presented here.

Cycle 17 was the first year a powerful new procedure was adopted for scheduling and optimizing parallel observations. Unlike previous cycles, each of the parallels teams was allowed to select individual observing opportunities, with accurately known durations of each orbital visit, well in advance. Since every parallel visit is unique, with its own combination of full and partial orbits, we optimized each individual orbit to obtain the exposure time ratios mentioned above in the available time, thereby reaching a carefully balanced set of sensitivities. This tremendous improvement over earlier years of "generic" parallel visits has improved the efficiency of our observing program by about 50% for a fixed allocation of orbits. We also requested, and were granted, an additional 17 single-orbit parallel observations. Although these were too short for the purposes of other programs, when we observe these new parallel fields in only the F140W and G_{141}, we are still able to reach comparable depths to the G_{141} images of many of our multi-orbit fields (See Table 1).

3. DATA REDUCTION

Slitless spectroscopy offers a considerable number of advantages for our WISP program. The high multiplexing capabilities

[9] http://www.stsci.edu/hst/wfc3/

Table 1
Schedule of Observations to Date for the WISP Survey

Field	Date	R.A. (HMS)	Decl. (DMS)	Number of Orbits	F110W (s)	G_{102} (s)	F140W (s)	G_{141} (s)	Primary Proposal ID	Primary Visit No.	Primary Instrument
1	2009 Nov 24	01 06 35.29	+15 08 53.8	4	884	4815	506	2609	11720	01	COS
5	2009 Dec 20	14 27 06.64	+57 51 36.2	5	1034	5515	1034	5515	11720	13	COS
6	2009 Dec 24	01 50 17.18	+13 04 12.8	4	609	3609	862	5015	11727	09	COS
7	2009 Dec 25	14 27 05.91	+57 53 33.7	7	834	6318	1112	6224	11720	14	COS
9	2009 Dec 29	12 29 44.31	+07 48 23.5	4	759	4612	684	3712	11703	01	STIS
10	2010 Jan 2	09 25 07.84	+48 57 03.0	3	631	3909	406	2209	11742	06	COS
11	2010 Jan 3	11 02 17.38	+10 54 25.4	3	556	3709	456	2006	11742	07	COS
12	2010 Jan 4	12 09 25.25	+45 43 19.8	5	1312	8221	606	3009	11741	04	COS
13	2010 Jan 9	01 06 38.77	+15 08 26.2	3	556	3009	506	2409	11720	03	COS
14	2010 Jan 9	02 34 56.80	−04 06 54.5	4	834	6215	481	2809	11741	03	COS
15	2010 Feb 12	14 09 42.47	+26 21 56.0	5	1612	8321	531	2609	11741	26	COS
16	2010 Feb 16	02 34 54.72	−04 06 42.5	5	1087	6921	584	2509	11741	01	COS
17	2010 Feb 18	02 13 38.11	+12 54 59.3	3	534	3409	559	3409	11727	11	COS
18	2010 Feb 19	12 29 17.25	+10 44 00.6	5	534	3512	762	3824	11561	04	COS
19	2010 Feb 20	02 34 54.29	−04 06 30.5	5	1187	8721	484	2809	11741	02	COS
20	2010 Feb 21	14 09 41.15	+26 22 15.1	7	1815	8430	559	2812	11741	25	COS
21	2010 Mar 5	09 27 55.77	+60 27 05.3	1	0	0	353	2006	11728	10	COS
22	2010 Mar 5	08 52 44.99	+03 09 09.6	1	0	0	253	1806	11728	13	COS
23	2010 Mar 6	09 43 16.12	+05 27 37.1	3	0	0	681	4115	11598	42	COS

Notes. A summary of the observations performed under the *HST* program GO/PAR 11696 for the WISP Survey to date. Four additional fields were deferred to a later paper, because they require additional reductions. Note that some targets have more than five orbits of observations. These are not necessarily all full orbits, however, which is why, for example, a three-orbit observation may have more than half the total integration time of a six-orbit observation, and targets with the same number of orbits have varying total integration times.

offered by the WFC3 grisms combined with the observation of a significant number of uncorrelated fields offered by the pure-parallel strategy make it perfectly suited for survey purposes. It allows a wide, uncontaminated spectral coverage with stable and accurate calibration. The ability to combine G_{102} and G_{141} grisms, with a well-behaved overlap, gives the unique opportunity to find multiple lines per object at faint magnitudes. Because of the well-behaved photometry, it is possible to combine the spectra with broadband photometry to provide comprehensive and precise spectral energy distribution. Moreover, the use of the *HST* offers a much lower sky background level compared to the ground. However, to fully exploit the potential of this tool, one needs to overcome some limitations. In crowded fields, object spectra and orders sometimes overlap, leading to confusion in the spectral extraction and to uncertainties in the background estimate. Given the high latitude of the WISP fields, crowding did not represent a problem in our observations. The spectral resolution is determined by the size of the target: for point-like sources, this corresponds to the instrument PSF, while for extended sources it is the spatial extent of the object in the dispersion direction.

This basic principle of the slitless reduction is the use of the direct images to provide the input catalog of objects. The object positions, sizes, and shapes are then used—in conjunction with a precise knowledge of the mapping between the direct and the dispersed frames to extract photometric and wavelength calibrated two-dimensional and one-dimensional spectra from the data using a three-dimensional flat-field cube which contains the calibration of each detector pixel for each wavelength. This process has been integrated with the WFC3 pipeline (CALWF3 version 2.0) with the provision of the aXe software (Kuemmel et al. 2009a) which has been developed to handle all of the *HST* slitless spectroscopic modes, beginning with ACS (Pirzkal et al. 2001). aXe maps not only the +first-order spectra but also the zeroth, −first, and +/−second and higher order spectra which allow the quantitative estimation of contamination in the case of overlapping objects.

We processed all the data (including both grism and direct imaging exposures) using the CALWF3 pipeline (version 2.0). Direct images were corrected for bias, dark, flat-field and gain variation using the best reference files obtained from the STScI archive. WFC3 performs multiple non-destructive reads in the slitless spectra in MULTIACCUM mode with the sampling sequence SPARS100. This allows cosmic ray rejection in a single exposure sequence. The reduction pipeline fits the accumulating signal in the MultiAccum readouts to identify the cosmic rays. In the slitless grism data, pixels cannot be associated with a unique wavelength. For this reason, CALWF3 applies a unity flat so that no pixel-to-pixel correction is applied at this stage. The proper flat fielding is then applied during the extraction of the spectra with aXe, using flat-field cubes generated during thermal vacuum (TV) 3 ground calibration of the WFC3 IR grisms (Kuntschner et al. 2008). G_{102} and G_{141} grisms were sampled over their respective wavelength ranges in steps of 200 Å. The flat fields were fitted pixel-by-pixel with wavelength and the fit residuals showed mean values of 0.8% and 0.6% for the G_{102} and G_{141} grisms, respectively.

3.1. Direct Images

Because our pure-parallel observations do not allow dithering, the processed images still contain a significant number of bad pixels that were not identified during the CALWF3 step. In addition, CALWF3 fails to properly flag a fraction of cosmic ray hits, when the impacted pixel causes an e^- bleeding into the adjacent pixels, with a typical cross pattern. This represents a fraction of 0.1% to 0.3 % of the total pixels. We identify the single affected pixel from the DQ file and then apply a sigma-clipping to the cross pattern, replacing the deviant pixels by the mean of the closest good ones. Then, the DQ extension

is updated. Finally, the images are combined with the IRAF task MULTIDRIZZLE (Koekemoer et al. 2002) using standard parameters. This step also corrects for bad pixels and cosmic rays and removes the geometric distortion using the latest distortion solution (IDCTAB) files. The final drizzled images have accurate astrometry and a uniform photometry across the image.

The position of the spectra in the dispersed images is determined by the location of the objects in the corresponding direct exposure. We run SExtractor (Bertin & Arnouts 1996) on the drizzled direct images, creating independent source catalogs for the F110W and F140W images. For the source detection, we used the rms weight maps derived during the MULTIDRIZZLE step. Every source in the catalog is required to have at least six connected pixels (DETECT_MINAREA = 6), with values above 3.5σ (DETECT_THRESH = 3.5σ). Finally, the catalogs generated for the F110W and F140W images are matched and put on the same numbering scheme. The individual detection in both filters allows us to keep objects detected in only one band and ensures an accurate astrometry between the grism image and the reference direct one. Because aXe performs the spectral extraction on individual (not distortion-corrected) grism frames, the combined catalog is projected back to these frames to generate an input object list (IOL) of coordinates for each grism frame to be used in the aXe extraction. Starting from these IOLs, the aXe software computes the reference position and spectral trace for each object in the dispersed images.

3.2. Grism Images

Before proceeding to the actual spectral extraction, the sky background must be estimated and subtracted from each grism frame. It is possible, within aXe, to estimate the background locally by interpolating on the sky regions above and below the spectral trace. However, we decided to perform a global sky subtraction on the entire image before proceeding to the extraction of the spectra. This method proves more efficient for slitless survey data (Pirzkal et al. 2004), where spectra may be contaminated by the trace of nearby objects, and multiple orders.

In the slitless mode, each spatial element of the detector receives the full sky and telescope foreground emission integrated over the grism bandpass. The grisms disperse the foreground light, but the lack of a slit results in a mapping of spatial to spectral domains that reintegrates uniform sources (e.g., the sky) effectively into undispersed emission. A portion of the detector does not receive the full zero-order sky and thus there is a ramp in the sky in the first one hundred or so columns on the detector. The sky foreground in the G_{141} and G_{102} grisms is a combination of zodiacal light, Earth limb, and thermal emission from the telescope. The processed two-dimensional grism images contain a significant signal from these sources that must be removed for proper photometric calibration, as well as for optimal identification of spectral features.

We constructed a master sky template for each grism by making a stack of all of our grism exposures. We started by removing the bright sources in the individual images by using the aperture beams created by aXe during the spectral extraction. This information is used to create a bad-pixel mask for each frame in an IRAF format. Then, the individual images were scaled using the image mode, then combined with a median stack using IMCOMBINE together with the bad-pixel file to mask out the regions affected by the spectral trace. The resulting master sky contains low-level residuals from bright extended sources, but these have little impact on our results. Our sky template is being improved as additional independent fields are observed and added to the master sky.

For each grism observation, we scaled the appropriate master sky and subtracted this from the post-pipeline two-dimensional image. We experimented with scaling the sky by the mode of the pixel distributions and by minimizing the sigma in the sky-subtracted image. These two approaches gave nearly identical results, and we proceeded with the skies scaled using the mode. The scale factors varied by more than a factor of 2 from one field to another, reflecting the changing zodiacal light background and contribution from Earth's limb. This temporal variation is the main source of uncertainty in the characterization of the sky background. After subtraction of the sky template from the grism frames, the typical residuals observed are about 10^{-2} e^{-} s^{-1} $pixel^{-1}$. The typical residuals in the calibrated spectra can be inferred from Figure 5. We adopted this sky-subtraction method after comparison to the one used by AXEPREP task, within aXe, to scale the background to the grism frames, and which shows slightly higher residuals.

As in the direct images, the CALWF3 processed data still showed residual bad pixels and cosmic rays. We constructed a bad-pixel mask in which we flagged all bad pixels, including those with low quantum efficiency and with high value of the dark current. We then interpolated over these flagged pixels along the dispersion direction using a second-order polynomial. We find that the majority of the bad pixels are isolated, and most interpolations were over at most 3 pixels. Thus, the interpolation step does not introduce spurious features into the spectra. Moreover, because the position of each bad pixel is recorded in the masks, we have checked that the identified emission lines (see below) were not impacted by the interpolation process. Finally, we created the final-dispersed images by averaging together the corrected frames, weighting each image by its exposure time. These frames were used in our visual inspection (cf. Section 3.4)

We also run MULTIDRIZZLE on the individual grism frames. This has the advantage of performing cosmic ray rejection and flagging the affected pixels in these frames. However, the drizzled grism image is not used for extraction. The aXe procedure extracts the spectra from the individual grism images and all flagged pixels will be ignored during this process. Another advantage of applying MULTIDRIZZLE on both direct and grism frames is to avoid potential differences in the world coordinate system data for the two images that could lead to a mismatch in the source positions in the direct and grism individual images during the extraction.

3.3. aXe Extraction

The spectral extraction is performed with the slitless extraction package aXe (version 2.0) developed at Space Telescope European Coordinating Facility (ST-ECF). The input image list is prepared with each individual grism image paired with the direct image which is closest in time and to its SExtractor catalog. We used the latest in-orbit configuration files (Kuntschner et al. 2009a, 2009b) and TV3 sensitivity calibrations. Some of these reference files will be improved for later reductions. We compared several apertures and orientation parameter setups to optimize the extraction. We used an aperture width of twice the object size listed in the IOL, and an extraction direction perpendicular to the spectral trace (see aXe user manual[10] for details).

[10] http://www.stecf.org/software/slitless_software/axe/

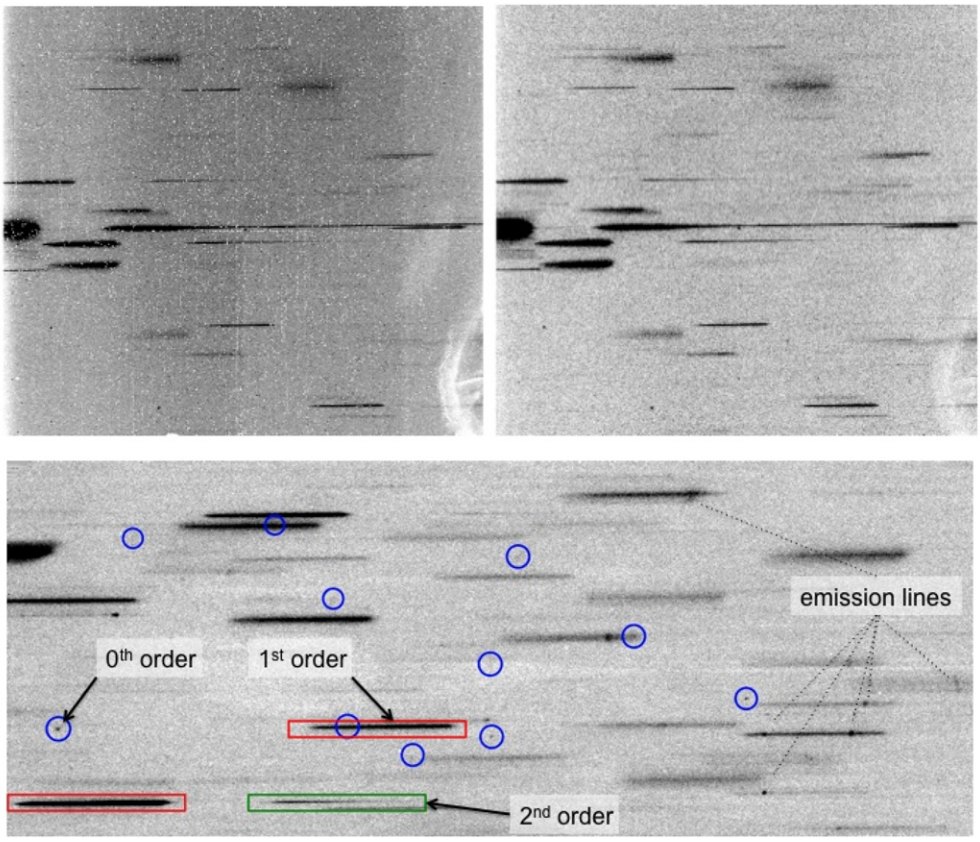

Figure 1. Top panel: a comparison of an individual G_{141} grism image before and after the reduction process, including background subtraction but not flat fielding. The raw image on the left shows a large number of bad pixels and cosmetic artifacts that are no longer visible on the clean image. Bottom panel: an example of different spectral features in our grism images. Red and green rectangles indicate examples of first- and second-order spectra, respectively. The blue circles mark the zero-order positions, indicating in some cases a contamination to the spectra. Some emission lines are also indicated.

(A color version of this figure is available in the online journal.)

Two-dimensional cutout spectra of each object in each exposure are extracted and then combined (with aXeDRIZZLE) to create a final high signal-to-noise ratio (S/N) spectrum. The combined two-dimensional spectrum is then used to extract the final object spectrum. We used optimal extraction to increase the (S/N) of the extracted spectra. The spectral contamination by spectra of nearby objects is estimated by aXe using the object positions and magnitudes in the direct image. We adopted the Gaussian emission model, using SExtractor size parameters, to approximate the object morphology. The simulated spectrum is then extracted and used to estimate the contamination to each object.

3.4. Emission-line Objects

Each stacked two-dimensional grism frame was searched visually by two or more of the authors. We adopted this approach, as preferred to the simple inspection of extracted one-dimensional spectra, because we identify easily emission lines and some remaining spurious features that could be misidentified as lines in the one-dimensional spectrum. Moreover, when we inspect the one-dimensional spectra, it happens that faint zeroth orders are not properly flagged by the contamination model of aXe, while it is clearly flagged in our two-dimensional visualization procedure (see below).

We used the dispersion solution from the WFC3 configuration files to determine the positions of the aperture beams in both grisms. The first order of each object is then marked with the corresponding aperture beam and the original ID number in the IOL. The actual search area is about 3.3 arcmin^2, smaller than the IR channel field of view. Because of the shift between direct and grism images, spectra on the left part of the field do not have detections in the direct image, and zeroth orders cannot be identified at the far-right side of the frame. Some examples of first- and second-order aperture beams are shown in Figure 1 by the long rectangular boxes.

Besides the overlap between the objects, the most important spurious feature is the zero-order image. Because the light is not dispersed, the zero-order image could be easily confused with an emission line. We derived the position of all the zero orders in the grism exposures, using the positions of all the sources in the direct images. We marked the zero orders in the grism exposures to be able to exclude them during the visual inspection of the grism images. In Figure 1, we show an example of this procedure: the blue circles show the zero-order location of some of the objects detected in the direct images. With all possible contaminants identified in the grism images, we proceeded to compile a list of all emission-line sources in each field. We compared the G_{102} and G_{141} spectra of each field side-by-side, to aid in the identification of genuine emission lines. In many cases, the identification of the lines is unambiguous. For example, galaxies with Hα often also have detectable [S II]6717/6731 and sometimes [S III]9069, 9532 emission (Figure 2). Strong [O III]5007, 4959 emission in the G_{102} grism is easily recognized on the basis of Hα in the G_{141} and often Hβ in the G_{102} spectra, even though the two [O III] lines are blended (see Figure 3). At higher redshifts, strong [O III]5007,4959 in the G_{141} grism is

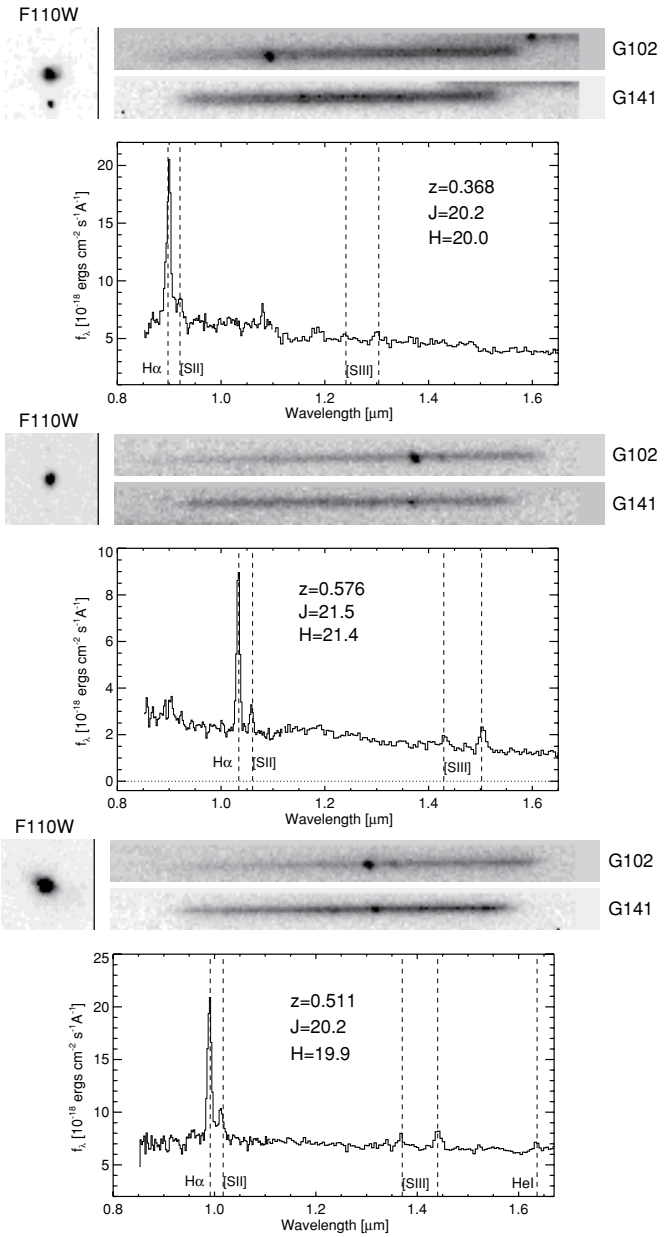

Figure 2. Examples I: low-redshift emission-line objects at $0.4 < z < 0.8$. For each object, we show the direct image cutout ($5'' \times 5''$), the two-dimensional G_{102} and G_{141} grism spectra and the one-dimensional extracted spectrum at observed wavelength. In this category, Hα falls in the G_{102} grism. We can see several emission lines: [S II]6716+6732 Å, [S III]9069 Å, [S III]9532 Å, and He I10830 Å.

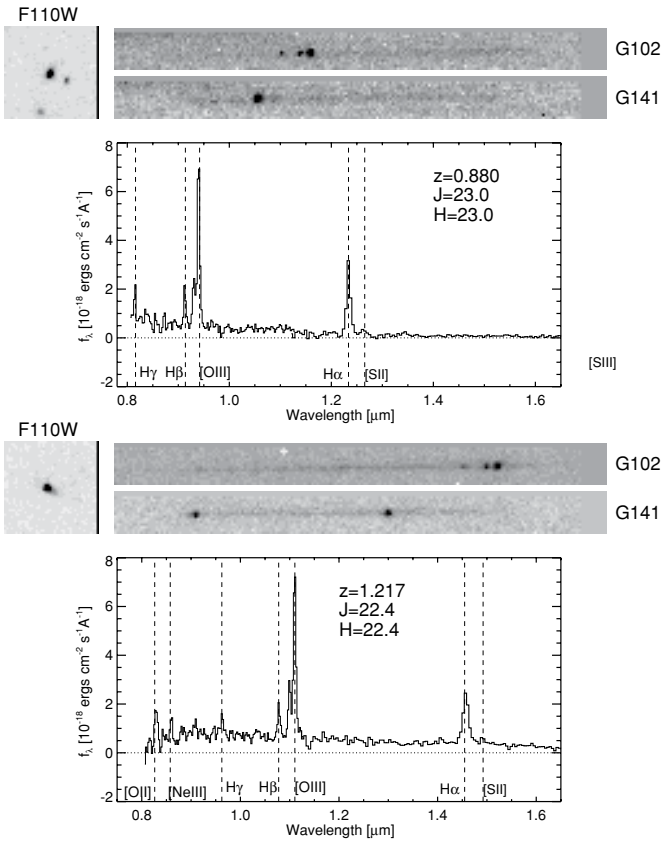

Figure 3. Examples II: emission-line objects in the redshift range $0.6 < z < 1.3$. For each object, we show the direct image cutout ($5'' \times 5''$), the two-dimensional G_{102} and G_{141} grism spectra, and the one-dimensional extracted spectrum at observed wavelength. This category includes mainly Hα[O III] line emitters, but we also observe [O II], [Ne III], Hβ, Hγ, and [S II]6716+6732 Å.

confirmed by faint Hβ emission. In some cases [O II]3727 can be seen in the G_{102} spectra for sources with strong [O III]5007 in the G_{141} spectra (Figure 4).

There are a large number of objects with only a single faint emission line in the full spectral range covered by the two grisms. It is most probable that these are weak Hα emission lines for which we are unable to detect other lines. However, since we see many [O III]/Hα pairs up to $z \sim 1.5$ we expect, in absence of other indications, to have a fraction of the single lines in the G_{141} that would correspond to [O III] whereas Hα has moved out of the G_{141} grism. The [O II]3727 line is seldom recognized as a redshift indicator by itself, since in this case it is more likely to be an Hα line at low-z rather than a high-z [O II] line. There are some objects, however, for which we believe the single line in the G_{141} spectrum is [O III]5007, 4959. This is primarily based on the lack of continuum in the G_{102} spectra, indicative of the fall off in the continuum below the Balmer and 4000 Å breaks.

Each emission feature was assigned a confidence flag, ranging from 0 to 4 in order of decreasing confidence. The highest confidence level (class 0) was assigned to objects with multiple emission features and unambiguous redshifts. Confidence classes 1– 3 were assigned to single features with unambiguous identifications (class 1), good quality (class 2), moderate quality (class 3), and uncertain (class 4, which are not included in the present analysis). Similar confidence classes have been used in ground-based redshift surveys (e.g., CFRS, Le Fevre et al. 1995; GDDS, Abraham et al. 2004) and have been found to be useful in restricting various types of analysis to high-confidence objects.

The final object catalog contains a measurement of each emission line, performed on the one-dimensional flux-calibrated spectra using a custom IDL fitting tool, and relevant information from the object extraction. The line fitting uses the pixel position of the identified lines, applies the grism dispersion solution to find the corresponding wavelength and therefore the redshift of the object. The fitting model consists of a polynomial continuum and a Gaussian (a multi-Gaussian model is used to deblend the Hα [SII] and [OIII]5007,4959 Å lines). The program fits the identified lines by least squares, and tries to fit potential lines that could be present in the spectrum at the correct redshift with a lower significance of typically 2σ. The entire process is visually monitored by displaying the line, the fit model,

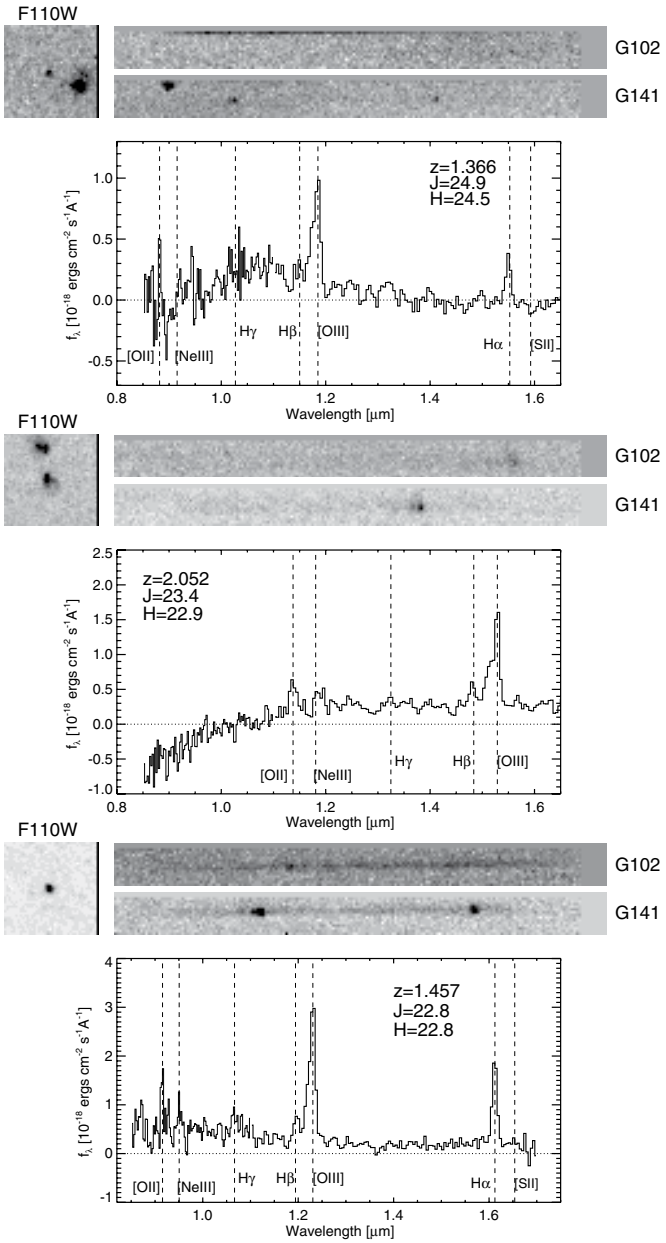

Figure 4. Examples III: high-redshift emission-line objects between $1.3 < z < 2.3$. For each object, we show the direct image cutout ($5'' \times 5''$), the two-dimensional G_{102} and G_{141} grism spectra and the one-dimensional extracted spectrum at observed wavelength. At these redshifts, both Hα and [O III] are shifted to the G_{141} grism. In many cases, we also observe the [O II] emission line in the G_{102} grism.

and the robustness of the fit. The fitting flux uncertainties are derived from our aXe extraction and calibration. As an independent check, a large subset of these same emission lines were also measured by hand, using the SPLOT task in IRAF. The resulting splot measurements generally agree with the automated measures to within the uncertainties.

We investigated the accuracy of the grism data calibration. First, we compared the fluxes of lines detected simultaneously in both G_{102} and G_{141} grisms in a wavelength domain restricted to a throughput higher than 10%. In most cases, the fluxes agree to better than 10% between the two grisms. Second, we compared the agreement between wavelength calibrations by using the overlapping region around 1.15 μm and the redshift determined independently from different lines detected in G_{102} and G_{141}. We observed a typical offset of 2×10^{-3} μm that is within the uncertainties of the redshift determination in the individual grisms. Overall, the final calibrated one-dimensional spectra have typical flux errors of 5%–20%. These uncertainties are representative of the high-throughput wavelength range of the two grisms, the errors being larger at the edges. For faint sources ($J_{110} > 23$), the continuum errors are in general larger. The flux uncertainty will also depends on the size of the source, and the grism calibration files will be improved with more observations to account for this effect. In most cases, we found very good agreement between the flux calibration of the two grisms. In the few cases of disagreement, the typical discrepancy observed between the red end of G_{102} and the blue end of G_{141} is still less than 50%. The broadband fluxes can be used to scale and reconcile the red and the blue grism spectra. To empirically estimate the accuracy of the grism flux calibration, we also compared the SExtractor broadband flux of the direct images to the synthetic flux measured from the grism calibrated spectra. The difference is typically less than 10%. This empirical estimate of the overall uncertainties involved in the spectral extraction shows the good flux calibration of our slitless spectra.

3.5. Grism Sensitivities

Due to the pure-parallel nature of our program, we have no control over the location and timing of our observations. Because of this, we are subject to a variety of visit durations (typically 3–5 orbits), number of readouts, and backgrounds (zodiacal light and earthshine), all of which affect the sensitivity of our observations. In order to determine the depth of our spectroscopy, we have measured the background rms (in electrons per second) of every final reduced grism image. This rms is then divided by the sensitivity (as a function of wavelength) and divided again by the dispersion (in Å pixel^{-1}) to give the 1σ noise as a function of wavelength. In Figure 5, we plot the 5σ continuum sensitivity in a five-pixel wide aperture (in the spatial direction) for each pointing. We used three pixel widths in the dispersion axis to estimate the line sensitivities. Each field has been scaled by (exptime)$^{1/2}$ so that the relative depths are comparable. Though most observations agree with the predicted depths from the WFC3 exposure time calculator, there is a large dispersion in the depths due to background variations, and any given field can vary substantially from the mean by typically 20% (up to ~50%). We also plot in Figure 6 our line sensitivity as a function of depth. In both grisms, we reach a median depth of about $\sim 5 \times 10^{-17}$ erg s^{-1} cm^{-2}.

In summary, for the typical exposure times of the survey (~6400 s in G_{102}, ~2700 s in G_{141}) we are able to detect (at 5σ) compact lines with $f = 5\times 10^{-17}$ erg s^{-1} cm^{-2} at $0.95 < \lambda < 1.17$ Å and $1.3 < \lambda < 1.65$ Å.

4. EMISSION-LINE RESULTS

To date, we have selected emission lines over 19 WFC3 fields, and measured redshifts and line fluxes from the highest confidence emitters. While incomplete at the faintest lines, we clearly reach emission-line fluxes down to 5×10^{-17} erg s^{-1} cm^{-2}, often in the presence of a second brighter line. At the highest confidence levels, our preliminary analysis yields 328 (S/N > 5) emission lines from 229 objects in our 19 WFC3 fields. Simulations will be required to determine our incompleteness due to extended emission confusion, and both high and low equivalent widths, while accounting for the non-uniform survey

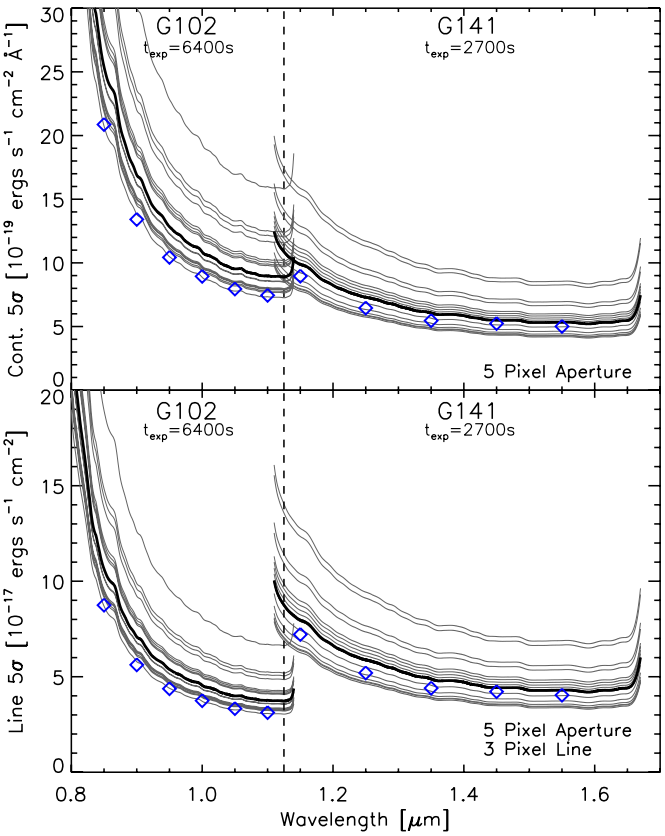

Figure 5. 5σ continuum (top) and line (bottom) sensitivities as a function of wavelength. The depth of each field is plotted in gray and scaled (by exptime$^{1/2}$) to the "nominal" survey exposure times. The thick solid lines denote the median field depth. The blue diamonds are the values given by the exposure time calculator assuming "average" earthshine and zodiacal light backgrounds. A five-pixel (0.″65) wide aperture was used for these estimates and the line sensitivities assumed three pixel widths in the dispersion direction. More compact sources will give slightly better sensitivities. There is significant scatter from the median due to variations in background levels.

(A color version of this figure is available in the online journal.)

Table 2
Emission Lines in the WISP Survey

Line	Number Detected
Single lines	129
Hα confirmed	56
Hβ	5
[O III]5007	59
[O III]4959	35
[O II]3727	15
[S II]6717 + 6731	15
[S III]9069	3
[S III]9532	5

Notes. The main emission lines with a signal-to-noise ratio S/N $\geqslant 5$ detected in the WISP Survey. Singles lines, without confirmation by another line, are assumed to be Hα.

sensitivity shown in Figure 5. We list the identifications of these lines in Table 2. We note that the fraction of sources with multiple emission lines increases if we include lines detected at 3σ–5σ, which represents about 10 objects so far in our survey. In the case of multiple emission-line objects, the less significant line (at 3σ) helps to identify the nature of the brighter one detected at higher significance level.

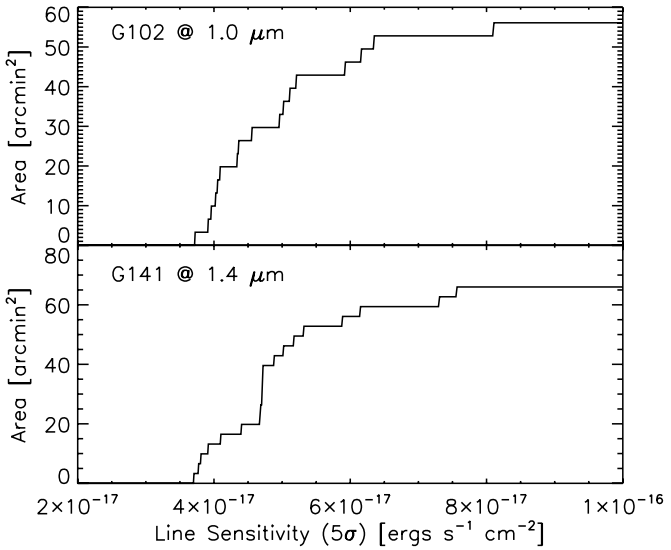

Figure 6. Cumulative area as a function of depth. Each field has an effective area of 3.3 arcmin^2 which is added to the cumulative area at the value of its 5σ line sensitivity (in a 5×3 pixel region). The depth varies as a function of wavelength so we choose to use the depths at the central wavelengths (1.0 μm for G_{102} and 1.4 μm for G_{141}). The depths are better at longer wavelengths and worse at lower wavelengths. The median depths in both grisms are $\sim 5 \times 10^{-17}$ erg s^{-1} cm^{-2}.

We find 185 galaxies with likely or definite Hα emission. Amongst these, 56 have secure identifications based on multiple emission lines. We also identify single-line objects as Hα emitters, as was the case with NICMOS grism spectroscopy (McCarthy et al. 1999; Hicks et al. 2002; Shim et al. 2009). This assumption has generally worked in ground-based narrowband IR detections of single emission lines (e.g., Bunker et al. 1995; Malkan et al. 1996; van der Werf et al. 2000; Sobral et al. 2009a).

Other possible line identifications would almost always result in a brighter line that we would also detect. The most significant possibility of a single emission line that is not Hα would be [O III] 5007+4959. This does occasionally happen in ground-based near-IR searches (Teplitz et al. 1999). Not surprisingly, for the remaining 56 objects with multiple bright emission lines, the most common combination is Hα + [O III] 4959/5007. The redshift distributions for the total sample are shown in the left panel of Figure 7, while the right-hand panel shows the redshift distribution for the Hα, [O III], and [O II] emitters separately.

We next compare these first results to our previous NICMOS Hα survey (McCarthy et al. 1999; Shim et al. 2009). With WFC3, we see Hα emission from $0.3 < z < 1.5$, whereas with the NICMOS G_{141} survey we were sensitive to Hα from $0.7 < z < 1.9$. In the left panel of Figure 8, we plot raw number counts for the Hα and single-line emitters separately (red and blue points, respectively) and then for the total (Hα + single-line) sample (black). We then compare total counts from both surveys, in the overlapping redshift range of $0.7 < z < 1.5$ (right panel). At the brighter end, we find a good agreement between the WISP Survey and the NICMOS grism results, even without including the many lines which we have identified with a lower S/N. But WFC3 starts to detect more galaxies than NICMOS at $f \sim 3 \times 10^{-16}$ erg s^{-1} cm^{-2}. Toward the faint end and the completeness limit of NICMOS, the surface density of Hα emitters detected with WFC3 is a factor of 3 higher. This is because our survey is more complete for extended line emission and our spectra are sensitive to a very wide range of emission line equivalent widths, from cases where the continuum is hardly detected (EW$_{\rm obs}$ > 300 Å; see Figure 9), to low contrast features

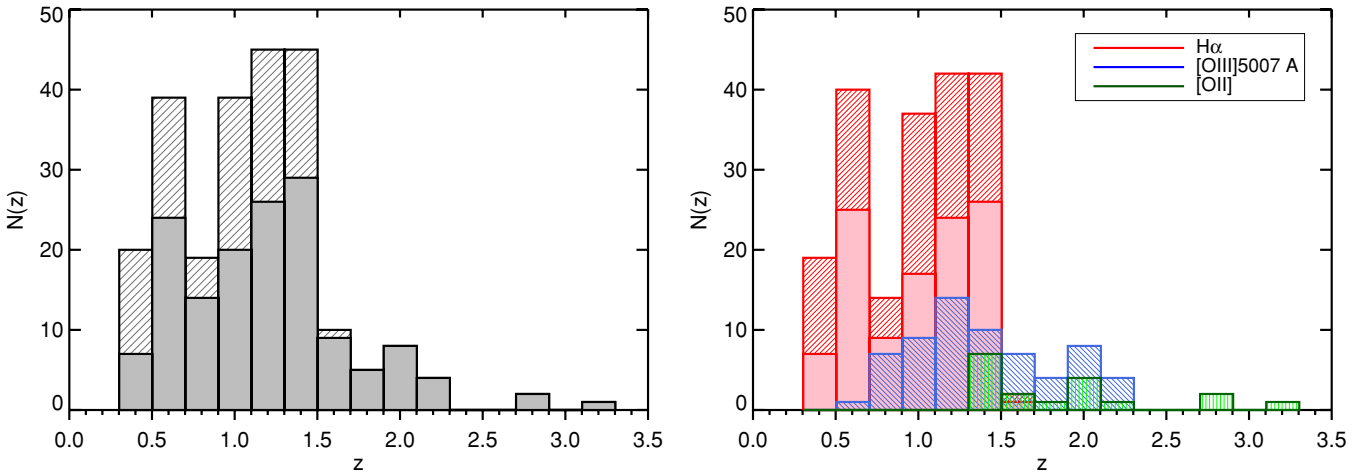

Figure 7. Left: the redshift distribution of our total sample of emission-line galaxies in 63 arcmin^2 of the WISP Survey. Filled histogram represents our secure redshift determination (classes 0 and 1), whereas on the top, the hatched part shows the uncertain single-emission-line objects assumed to be Hα emitters. Right: the redshift distribution of our galaxies according to their emission lines. Again the hatched part of the Hα emitters represents uncertain redshifts.

(A color version of this figure is available in the online journal.)

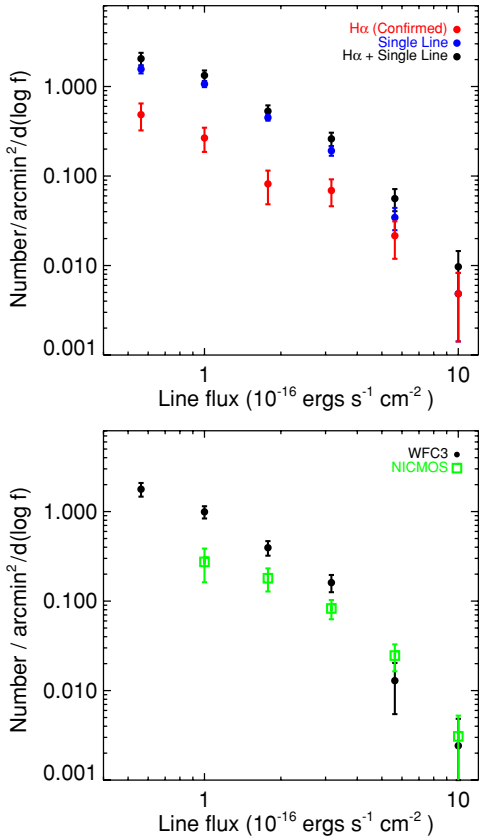

Figure 8. Top: number counts of Hα emitters in the WISP Survey. Confirmed Hα emitters are shown in red points, single-line emitters in blue, and the total counts in black. Bottom: number counts of Hα and single-line emitters in the WISP Survey (black points) compared to the NICMOS Parallel grism survey (green squares), tabulated in the overlapping redshift range of $0.7 < z < 1.5$. Counts are given per $d(\log f) = 0.25$.

(A color version of this figure is available in the online journal.)

with EW as low as 15 Å for lines that satisfy S/N = 5σ. However, the number counts presented here are still affected by incompleteness and this will be addressed in a forthcoming paper on the luminosity functions when our survey is complete (A. J. Bunker et al. 2011, in preparation).

As Figure 10 illustrates, we routinely detect emission lines in galaxies with luminosities well below L^*. Many of these very faint galaxies have strong [O III]5007 emission and relatively weak [O II] and Hβ emission, suggestive of low metal abundances. The near-IR photometry provided by our F110W and F140W images, and ground-based follow-up (where practical), will allow us to extend pioneering work on the mass–metallicity relation at $0.5 < z < 1$ (Savaglio et al. 2005) and $1 < z < 3$ (Erb et al. 2006) to significantly lower stellar masses. The mass–metallicity relation is a critical diagnostic of galaxy formation and evolution models as it is sensitive to a number of physical process (e.g., infall, supernovae (SNe) feedback, and initial mass function (IMF)).

In Figure 11, we plot on the left panel the observed SFR distribution of our Hα sample derived from the Hα luminosity using the Kennicutt (1998) conversion. Following Shapley et al. (2005), we corrected the Hα fluxes for 20% average [N II]6584+6548 contribution, but no extinction correction is applied. On the right panel, we plot SFR(Hα) versus rest-frame R-band luminosity. For rest wavelength R magnitudes, we used the F110W photometry if the observed wavelength of Hα is $<1.25\,\mu$m ($z < 0.9$) and the F140W photometry for Hα $> 1.25\,\mu$m ($z > 0.9$), applying only the $(1+z)$ correction (without any k-correction). There is no extinction correction for the R-band magnitudes. The median SFR is 4 $M_\odot$ yr^{-1}, and the median M_R of line-detected galaxies is -20.75, one and half magnitudes below $L^\star$ for $z \sim 1.0$ (Chen et al. 2003; Colbert et al. 2006). At the lower redshifts, especially for compact objects, our survey is able to detect lines in extraordinarily faint galaxies ($M_R > -19$), and SFRs less than 1 solar mass per year.

4.1. Absorption-line Spectra

Although we have so far limited the analysis to emission lines, the broad wavelength coverage and high sensitivity of the WISP Survey leads also to a wealth of information from continuum spectra. The 4000 Å break and the convergence of the Balmer series at 3650 Å provide two of the best low-resolution diagnostics for redshift and stellar populations. Continuum spectral diagnostics, particularly at $z > 1$, provide constraints on the mean age of the stellar population and the time since the last major episode of star formation. Spectroscopy of red galaxies

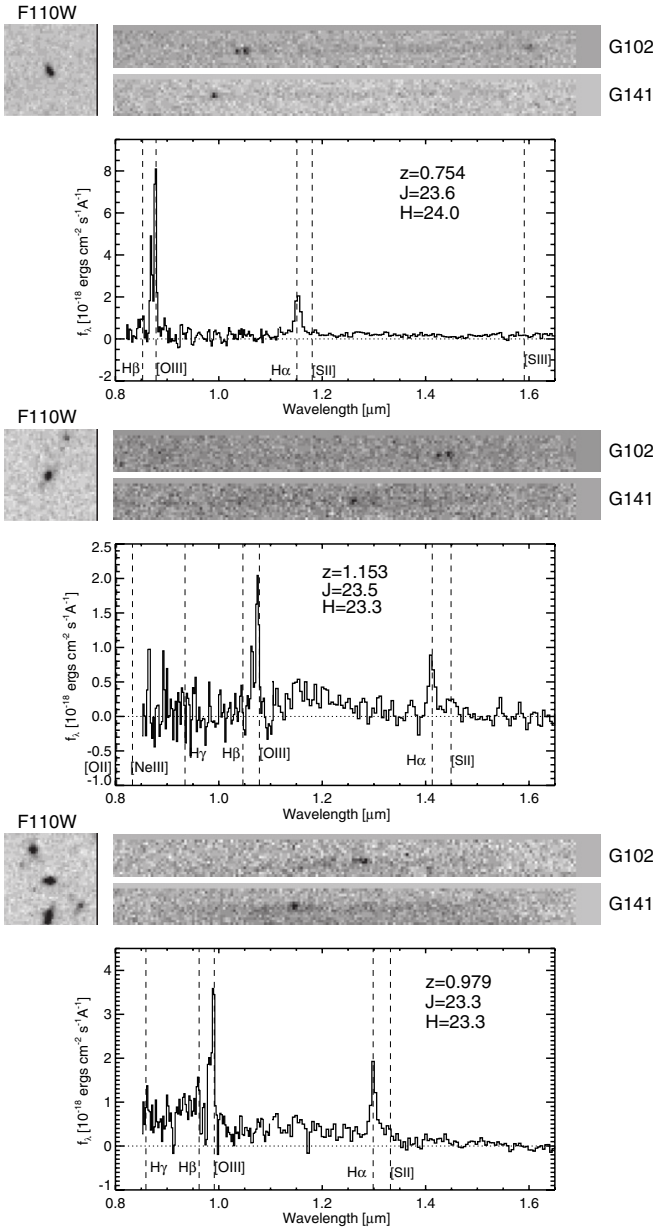

Figure 9. Examples IV: very high equivalent width emission-line objects. Strong emission lines are observed in this group of galaxies with an extremely faint continuum which is barely visible in the two-dimensional grism images. The observed EWs for objects from top to bottom are as follows: ($EW_{[O\,III]4959}$ = 600 Å, $EW_{[O\,III]5007}$ = 1550 Å, $EW_{H\alpha}$ = 800 Å); ($EW_{[O\,III]4959}$ = 490 Å, $EW_{[O\,III]5007}$ = 1130 Å, $EW_{H\alpha}$ = 520 Å); ($EW_{[O\,III]4959}$ = 150 Å, $EW_{[O\,III]5007}$ = 480 Å, $EW_{H\alpha}$ = 450 Å).

from the ground in the visible is limited to objects with $z < 1.8$ and $I < 25$ (e.g., McCarthy et al. 2004; Cimatti et al. 2004; Doherty et al. 2005). Near-IR spectroscopy can probe to higher redshifts, but this is quite challenging (e.g., Kriek et al. 2008) and has been limited to small samples to date (e.g., Doherty et al. 2006). The WFC3 grisms are providing low-resolution continuum spectroscopy of red galaxies in large numbers with great sensitivity (e.g., van Dokkum & Brammer 2010). In Figure 12, we show an example of a post-starburst galaxy at redshift $z = 1.68$. A clear Balmer break is seen in the G_{102} spectrum, as well as absorption lines in the G_{141} part. A stellar population model with an age of 600 Myr and an extinction of $A_V = 1.2$ is overplotted as a qualitative fit to the observed

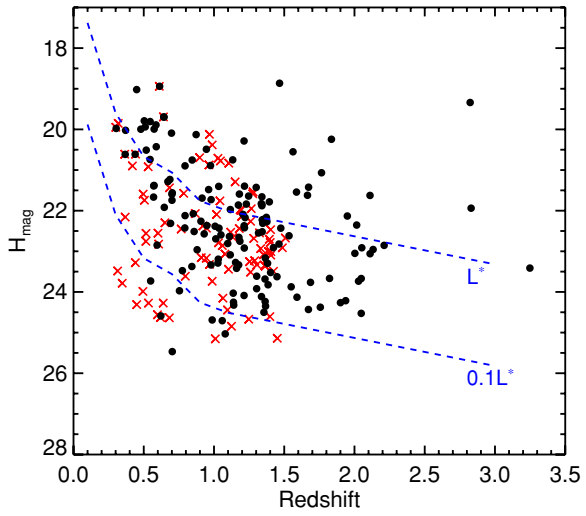

Figure 10. H_{140}-band magnitude as a function of redshift. Secure redshifts are shown as black circles and single-line (assumed to be Hα) emitters as red crosses. We also show the apparent H_{140}-band magnitude for $L^\star$ (and 0.1 $L^\star$) galaxies derived from rest-frame near-IR (at low-z) and optical (at $z > 0.7$) luminosity functions (Bell et al. 2003; Faber et al. 2007; Shapley et al. 2001).

(A color version of this figure is available in the online journal.)

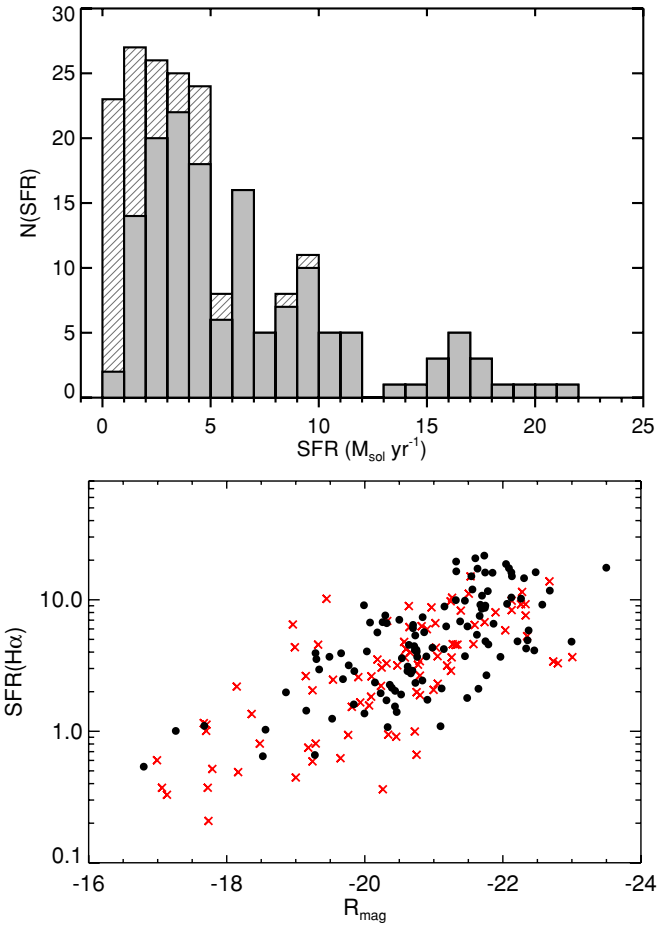

Figure 11. Top: observed star formation rate distribution of our Hα emitters. The Hα flux is reduced to account for 20% of [N II] contamination and converted to SFR using Kennicutt (1998) relation. The sample is split into high-z (shaded area) and low-z (hatched) sub-samples, where the separation between the two categories is $z = 0.675$. Bottom: SFR as a function of absolute R-band magnitude derived from F110W and F140W photometry for Hα emission below and above 1.25 μm, respectively. Black points represent confirmed Hα emitters and red crosses the single-line galaxies.

(A color version of this figure is available in the online journal.)

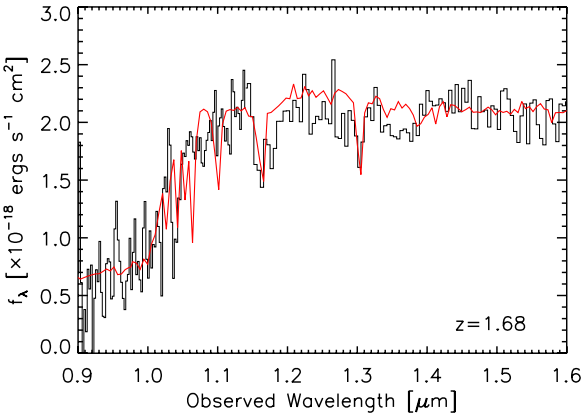

Figure 12. Example V: spectrum of a post-starburst galaxy at $z = 1.68$. A clear Balmer break can be seen in the G_{102} spectrum between $1.0 < \lambda < 1.1\,\mu$m as well as Balmer absorption lines in the G_{141} spectrum at 1.17 and 1.3 μm. Plotted (in red) is a Bruzual & Charlot (2003) stellar population model with an age of 600 Myr (e-folding time of 100 Myr), $A_V = 1.2$ mag (assuming a Calzetti reddening curve), and a Salpeter IMF.

(A color version of this figure is available in the online journal.)

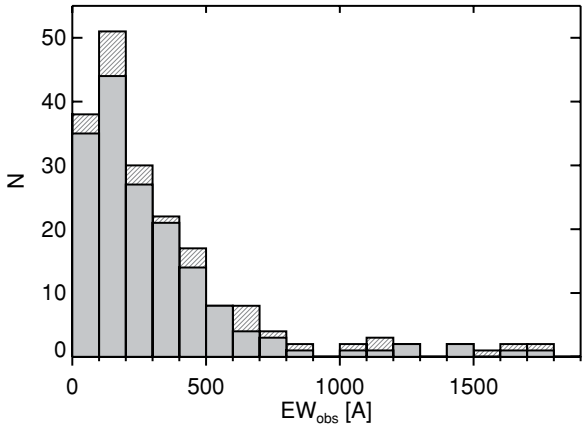

Figure 13. Equivalent width distribution of Hα (gray) and O III (hatched) emission lines in our sample. A significant number of objects show extremely high equivalent width lines, exceeding 300 Å.

spectrum. This object has been pre-identified searching for galaxies with H_{140}(AB) < 22 and $J_{110} - H_{140} > 0.6$. This selection isolates bright passive galaxies at $z > 1$.

5. DISCUSSION AND SUMMARY

We have presented the first analysis of the WISP Survey of slitless spectroscopy with the NIR channel of WFC3, taken in pure-parallel mode. In the first 19 fields, we surveyed 63 arcmin^2. At the highest confidence level, we have detected 229 emission-line objects. We reach typical 5σ sensitivities of $f \sim 5 \times 10^{-17}$ erg s^{-1} cm^{-2} for compact lines.

While wide-field narrowband imaging surveys from the ground (e.g., Sobral et al. 2009a; Momcheva et al. 2010) yield samples of Hα emitters that are larger than ours and near-IR slit spectroscopy of selected targets can yield emission-line ratios to faint levels (e.g., Pettini et al. 2001), the WFC3 grisms offer a unique opportunity to obtain continuous spectral coverage in the 0.8–1.7 μm region with high sensitivity. Our early results show that we can identify star-forming galaxies with space densities comparable to, or larger than, those identified with color selection techniques (e.g., BM/BX or Lyman Break Galaxy (LBG) selection; Adelberger et al. 2004) to similar SFR thresholds (Shapley et al. 2005; Erb et al. 2006). The typical emission-line galaxy at $z > 1.3$ in our sample has strong [O III]5007,4959 emission and a large [O III]/Hβ ratio, similar to the ratios seen in the small number of LBGs at $z > 1.5$ with rest-frame optical spectra (Pettini et al. 2001; Teplitz et al. 2000; Lemoine-Busserolle et al. 2003; Maiolino et al. 2008; Hainline et al. 2009). Coupled with the high [O III]/Hα ratio and weak [O II]3727 emission, these suggest low metal abundances. Future papers from our survey will examine line ratios and their implications for abundances and ionization sources. With the support of our ongoing ground-based, follow-up observing programs, we will be able to measure the mass–metallicity relation at crucial intermediate redshifts, to derive the Hα luminosity function at different redshifts and to study the evolution of the SFR density.

Many of our fields contain emission-line objects with extremely high equivalent widths (cf. Figure 7). In particular, more than 60 emission lines show equivalent widths higher than 300 Å. We show in Figure 13 the EW distribution of our Hα (gray) and O III (hatched) emitters. These strongly star-forming emission-line-dominated objects are reminiscent of the ultra-strong emission-line galaxies at $0 < z < 1$ discovered by Kakazu et al. (2007; see also Hu et al. 2009) and the "green pea" galaxies found in Sloan Digital Sky Survey by Cardamone et al. (2009). Prominent emission-line galaxies (eGRAPES) have been also selected using ACS grism spectroscopy by Pirzkal et al. (2006). These objects have metallicities comparable to the lowest observed in local sources and may be dwarf galaxies undergoing their first major star formation episode.

The sensitivity and resolution of the G_{102} grism also provide the opportunity to search for Lyα emission lines in addition to the rest-frame optical emission lines discussed here. We have excluded such analysis from the present paper given the limitations of the initial, visual selection of faint emission lines. After further analysis, WFC3 will offer a significant new approach to high-redshift ($z > 6$) searches for Lyα. Though extensive ground-based narrowband searches for Lyα-emitters have been performed up to $z = 7$, with the most distant confirmed source at $z = 6.96$ (Iye et al. 2006), it is difficult beyond this redshift to find wavelengths with both high sky transmission and low sky emission. Thus, many surveys are limited to a very small range at $z = 7.7$ or $z = 8.8$ (e.g., Sobral et al. 2009b), without any reliable Lyα emission-line candidates.

One of the original WISP goals has been to reach sufficient depths to detect possible Lyman-alpha emission line emitters (LAEs). Based on previous LAE studies at $z = 5.7$ and 6.6 (Shimasaku et al. 2006; Kashikawa et al. 2006), this requires detecting high equivalent width lines fainter than 5×10^{-17} erg s^{-1} cm^{-2}, our nominal depth at $\sim$1 μm, in 6400 s integration. This requirement is a main reason that such a large portion of the total observing time in our longer parallel opportunities is devoted to the G_{102} grism exposures. Several of the fields we present have more than 8000 s of G_{102} integration, and some new WISP observations have more than 10,000 s. Another advantage is that most of the faintest high-EW line emitters are very compact, only marginally resolved in either the spatial or wavelength dimensions. Therefore, we will be able to detect lines of 3×10^{-17} in many of our deeper G_{102} fields. The largest advantage we will have in this, however, is that the current paper only presented emission line detections of high confidence. Our ongoing work on lines detected with moderate confidence indicates that we will ultimately cover many tens

of square arcminutes down to (1–2) $\times 10^{-17}$ flux limits. If we achieve this, we will have a chance to detect LAE's out to $z \sim 9$, at least if they are as numerous as at lower redshifts. By obtaining comparably deep grism spectra at longer wavelengths, we should be able to rule out contaminants at moderate redshifts ([O II], [O III], Hα) when we have only strict upper limits to the presence of lines at their expected positions.

In addition to the WISP Survey, two large observing programs with the WFC3 grisms will contribute significant results. First, a G_{141} survey of the GOODS North fields is underway (GO-11600; PI = Weiner), reaching depths comparable to or slightly better than WISP. Secondly, the CANDELS multicycle treasury program (GO-12060 through 12064; PI = Faber and Ferguson) will obtain deep spectroscopy of selected pointings targeted to follow-up SNe found in direct imaging. The WISP Survey has some limitations compared to these programs due to the parallel mode, including the lack of dithering, but our first analysis demonstrates the great efficiency of this use of the telescope. WFC3 parallels can obtain large spectroscopic samples of emission-line objects during the peak epoch of star formation, free from the most common selection biases.

We gratefully acknowledge the dedicated efforts of several staff members at the Space Telescope Institute to make the new Grism Parallel observations as successful as possible. In particular, we thank Galina Soutchkova, Iain Neill Reid, Larry Petro, Karla Peterson, Denise Taylor, Kenneth Sembach, Bill Workman, Claus Leitherer, John MacKenty, Howard Bushouse, Ron Downes, and Alan Patterson. We thank the ST-ECF team of Martin Kümmel, Harald Kuntschner and Jeremy Walsh for their help with the data reduction and spectrum extraction processes and advice about the WFC3 calibration status. We also acknowledge the important contributions to supporting parallel observations by the late Roger Doxey.

REFERENCES

Adelberger, K. L., et al. 2004, ApJ, 607, 226
Abraham, R. G., et al. 2004, AJ, 127, 2455
Bell, E. F., McIntosh, D. H., Katz, N., & Weinberg, M. D. 2003, ApJS, 149, 289
Bertin, E., & Arnouts, S. 1996, A&AS, 117, 393
Bruzual, G., & Charlot, S. 2003, MNRAS, 344, 1000
Bunker, A. J., Warren, S. J., Hewett, P. C., & Clements, D. L. 1995, MNRAS, 273, 513
Cardamone, C., et al. 2009, MNRAS, 399, 1191
Chen, H.-W., et al. 2003, ApJ, 586, 745
Cimatti, A., et al. 2004, Nature, 430, 184
Colbert, J. W., Malkan, M. A., & Rich, R. M. 2006, ApJ, 648, 250
Daddi, E., et al. 2005, ApJ, 626, 680
Daddi, E., et al. 2007, ApJ, 670, 156
Doherty, M., Bunker, A. J., Ellis, R. S., & McCarthy, P. J. 2005, MNRAS, 361, 525
Doherty, M., Bunker, A., Sharp, R., Dalton, G., Parry, I., & Lewis, I. 2006, MNRAS, 370, 331
Drozdovsky, I., Yan, L., Chen, H.-W., Stern, D., Kennicutt, R., Jr., Spinrad, H., & Dawson, S. 2005, AJ, 130, 1324
Erb, D., Shapley, A., Pettini, M., Steidel, C., Reddy, N., & Adelberger, K. 2006, ApJ, 644, 813
Faber, S. M., et al. 2007, ApJ, 665, 265
Freudling, W., et al. 2008, A&A, 490, 1165
Gallego, J., Zamorano, J., Rego, M., Alonso, O., & Vitores, A. G. 1996, A&AS, 120, 323
Gardner, J. P., et al. 1998, ApJ, 492, L99
Hainline, K. N., Shapley, A. E., Kornei, K. A., Pettini, M., Buckley-Geer, E., Allam, S. S., & Tucker, D. L. 2009, ApJ, 701, 52
Hicks, E. K. S., Malkan, M. A., Teplitz, H. I., McCarthy, P. J., & Yan, L. 2002, ApJ, 581, 205
Hopkins, A. M. 2004, ApJ, 615, 209
Hopkins, A. M., Connolly, A. J., & Szalay, A. S. 2000, AJ, 120, 2843
Hu, E. M., Cowie, L. L., Kakazu, Y., & Barger, A. J. 2009, ApJ, 698, 2014
Iye, M., et al. 2006, Nature, 443, 186
Kakazu, Y., Cowie, L. L., & Hu, E. M. 2007, ApJ, 668, 853
Kashikawa, N., et al. 2006, ApJ, 648, 7
Kennicutt, R. C., Jr. 1998, ARA&A, 36, 189
Kimble, R. A., MacKenty, J. W., O'Connell, R. W., & Townsend, J. A. 2008, Proc. SPIE, 7010, 43
Kriek, M., et al. 2008, ApJ, 677, 219
Koekemoer, A. M., Fruchter, A. S., Hook, R. N., & Hack, W. 2002, in The 2002 HST Calibration Workshop: Hubble after the Installation of the ACS and the NICMOS Cooling System, ed. S. Arribas, A. Koekemoer, & B. Whitmore (Baltimore, MD: STScI), 337
Kuemmel, M., Walsh, J. R., Pirzkal, N., Kuntschner, H., & Pasquali, A. 2009a, PASP, 121, 59
Kuemmel, M., et al. 2009b, in ASP Conf. Ser. 411, Astronomical Data Analysis Software and Systems XVIII, ed. D. A. Bohlender, D. Durand, & P. Dowler (San Francisco, CA: ASP), 430
Kuntschner, H., Bushouse, H., Kuemmel, M., & Walsh, J. R. 2009a, ST-ECF ISR WFC3-2009-18 WFC3 SMOV Proposal 11552: Calibration of the G_{102} grism
Kuntschner, H., Bushouse, H., Kuemmel, M., & Walsh, J. R. 2009b, ST-ECF ISR WFC3-2009-17 WFC3 SMOV Proposal 11552: Calibration of the G_{141} Grism
Kuntschner, H., Bushouse, H., Walsh, J. R., & Kmmel, M. 2008, ST-ECF Instrument Science Report WFC3-2008-16: The TV3 Ground Calibrations of the WFC3 NIR Grisms
Le Fevre, O., Crampton, D., Lilly, S. J., Hammer, F., & Tresse, L. 1995, ApJ, 455, 60
Lemoine-Busserolle, M., Contini, T., Pelló, R., Le Borgne, J.-F., Kneib, J.-P., & Lidman, C. 2003, A&A, 397, 839
Maiolino, R., et al. 2008, A&A, 488, 463
Malhotra, S., et al. 2005, ApJ, 626, 666
Malkan, M., Teplitz, H., & McLean, I. 1996, ApJ, 468, L9
McCarthy, P., et al. 1999, ApJ, 520, 548
McCarthy, P. J., et al. 2004, ApJ, 614, L9
Momcheva, I., Lee, J., Ly, C., Salim, S., Dale, D., Garcia, C., Finn, R., & Ouchi, M. 2010, BAAS, 41, 559
Pasquali, A., et al. 2006, ApJ, 636, 115
Pettini, M., Shapley, A. E., Steidel, C. C., Cuby, J.-G., Dickinson, M., Moorwood, A. F. M., Adelberger, K. L., & Giavalisco, M. 2001, ApJ, 554, 981
Pirzkal, N., Malhotra, S., Rhoads, J. E., & Xu, C. 2007, ApJ, 667, 49
Pirzkal, N., Pasquali, A., & Demleitner, M. 2001, ST-ECF Newsletter, 29 Extracting ACS Slitless Spectra with aXe, 5
Pirzkal, N., et al. 2004, ApJS, 154, 501
Pirzkal, N., et al. 2006, ApJ, 636, 582
Rhoads, J. E., et al. 2005, ApJ, 621, 582
Savaglio, S., et al. 2005, ApJ, 635, 260
Shapley, A. E., Coil, A. L., Ma, C.-P., & Bundy, K. 2005, ApJ, 635, 1006
Shapley, A. E., Steidel, C. C., Adelberger, K. L., Dickinson, M., Giavalisco, M., & Pettini, M. 2001, ApJ, 562, 95
Shim, H., Colbert, J., Teplitz, H., Henry, A., Malkan, M., McCarthy, P., & Yan, L. 2009, ApJ, 696, 785
Shimasaku, K., et al. 2006, PASJ, 58, 313
Sobral, D., et al. 2009a, MNRAS, 398, 75
Sobral, D., et al. 2009b, MNRAS, 398, L68
Straughn, A. N., et al. 2008, AJ, 135, 1624
Straughn, A. N., et al. 2009, AJ, 138, 1022
Teplitz, H., Malkan, M., & McLean, I. 1999, ApJ, 514, 33
Teplitz, H. I., Collins, N. R., Gardner, J. P., Hill, R. S., Heap, S. R., Lindler, D. J., Rhodes, J., & Woodgate, B. E. 2003a, ApJS, 146, 209
Teplitz, H. I., Collins, N. R., Gardner, J. P., Hill, R. S., & Rhodes, J. 2003b, ApJ, 589, 704
Teplitz, H. I., et al. 2000, ApJ, 533, L65
van der Werf, P. P., Moorwood, A. F. M., & Bremer, M. N. 2000, A&A, 362, 509
van Dokkum, P. G., & Brammer, G. 2010, ApJ, 718, 73
Yan, L., McCarthy, P., Freudling, W., Teplitz, H., Malumuth, E., Weymann, R., & Malkan, M. 1999, ApJ, 519, 47
Yan, L., McCarthy, P., Weymann, R., Malkan, M., Teplitz, H., Storrie-Lombardi, L., Smith, M., & Dressler, A. 2000, AJ, 120, 575